Control Engineering Practice 21 (2013) 1110–1120

Contents lists available at SciVerse ScienceDirect

Control Engineering Practice

journal homepage: www.elsevier.com/locate/conengprac

Integrated design of the feedback controller and topography estimator for atomic force microscopy

S. Kuiper [a,*], P.M.J. Van den Hof [b,c], G. Schitter [d]

[a] TNO Technical Sciences, Stieltjesweg 1, 2628 CK Delft, The Netherlands
[b] Delft Center for Systems and Control Delft University of Technology, Mekelweg 2, 2628 CD Delft, The Netherlands
[c] Control Systems Group, Department of Electrical Engineering, University of Technology Eindhoven, Den Dolech 2, 5612 AZ Eindhoven, The Netherlands
[d] Automation and Control Institute, Vienna University of Technology, Gusshausstrasse 27–29, 1040 Vienna, Austria

ARTICLE INFO

Article history:
Received 4 October 2012
Accepted 19 March 2013

Keywords:
Atomic force microscopy
Model-based control
Robust control
Topography estimation
Optimal filter design

ABSTRACT

In atomic force microscopy (AFM) the force between the measurement tip and the sample is controlled in a feedback loop to prevent damage of the tip and sample during imaging, and to convert the measurement of the tip–sample force into an estimate of the sample topography. Dynamical uncertainties of the system limit the achievable control bandwidth and the accuracy of the topography estimation. This paper presents an integrated approach to design a feedback controller and topography estimator, taking into account the dynamical uncertainties of the system. The proposed methodology is experimentally demonstrated on a commercial AFM system, showing a direct trade-off between the control bandwidth and the accuracy of the topography estimation.

1. Introduction

Since its invention in 1986 (Binnig, Quate, & Gerber, 1986) the atomic force microscope (AFM) has become a very important tool in micro-biology, material science, and nanotechnology to measure various sample properties at the nanometer scale. In Fig. 1 the working principle of the AFM is depicted. The sample is probed by a very sharp tip that has an end-radius on the order of a few nanometers, which is mounted on the free end of a micro-cantilever. When the tip is brought in close proximity to the sample, the interaction forces between the tip and the sample can be detected by measuring the deflection of the cantilever beam via an optical sensing system (Alexander et al., 1989). During imaging the sample is scanned relative to the measurement tip in a lateral raster scanning pattern in order to image the area of interest. During scanning the interaction force between the tip and the sample is controlled by a feedback loop, manipulating the distance between the tip and the sample based on the measured cantilever deflection. This feedback loop prevents damage of the tip and the sample due to large interaction forces, and also allows us to convert the force measurement into an estimate of the sample topography. In order to provide the lateral scanning motion and to allow the control of the tip–sample interaction force, a high precision positioning stage is used that can position the sample relative to the measurement tip in all the three spatial directions. While scanning, the measured cantilever deflection and the compensating actions of the feedback loop are recorded by the system's data acquisition in order to obtain a map of the sample topography.

The blockdiagrams (a)–(c) of Fig. 2 (solid lines) depict the feedback loop in AFM controlling the tip–sample force, with the actuator dynamics G and the feedback controller K. The dynamics of the cantilever, the tip–sample interaction and the optical cantilever deflection detection are governed by B. While scanning, the sample topography enters the feedback loop as an unknown input signal, denoted $h(t)$ in Fig. 2. Signal $n(t)$ in Fig. 2 denotes the noise and disturbances acting on the system, which may be stemming from various sources, such as electronic noise from the sensor electronics and power amplifier, vibrations stemming from the environment, temperature drifts within the instrument, and Brownian noise observable from the small cantilever (Sarid, 1994). Although stemming from various sources, these noise contributions can be viewed as a signal entering the feedback loop at the same location as the sample topography signal $h(t)$.

During imaging, the feedback controller is aimed to minimize the variations of the tip–sample force with respect to the constant setpoint level r, in some sense minimizing the control error $e(t)=r-d(t)$. Due to this feedback action, the actuator follows the varying sample topography over the scanned area; $h(t)\approx -x(t)$ as long as $e(t)\approx 0$.

Different methods can be used to estimate the sample topography in AFM, as outlined by the different blockdiagrams of Fig. 2.

* Corresponding author. Tel.: +31 (0)888664806.
E-mail addresses: stefan.kuiper@tno.nl (S. Kuiper), p.m.j.vandenhof@tue.nl (P.M.J. Van den Hof), schitter@acin.tuwien.ac.at (G. Schitter).

0967-0661/$ - see front matter © 2013 Elsevier Ltd. All rights reserved.
http://dx.doi.org/10.1016/j.conengprac.2013.03.006

In most commercial AFM systems the sample topography is estimated by taking a calibrated scaling of the feedback controller output; $\hat{h}(t) = -\gamma \cdot u(t)$, as shown in Fig. 2a. The scaling factor γ maps the voltage output of the feedback controller towards the displacement of the actuator, and is obtained via calibration experiments (Easton & West, 2010). Although this method allows for low noise, and thus precise estimation of the sample topography, the accuracy of this approach is limited due to the fact that the actuator dynamics are neglected. When increasing the bandwidth of the feedback loop the higher frequency resonances within the actuator dynamics are excited, which influence the accuracy of the topography estimation if not accounted for. In Schitter, Menold, Knapp, Allgöwer, and Stemmer (2001) a method is discussed to improve the accuracy of the topography estimate by simulating the sample profile based on a model of the higher order actuator dynamics: $\hat{h}(t) = -\hat{x}(t) = -\hat{G}(p)u(t)$, with $\hat{G}(p)$ being a model of the actuator dynamics, and $p = d/dt$ the differential operator.

Hysteresis within the piezo-actuators may be another source of inaccuracy, which has been addressed in Fleming (2010) by compensating for the actuator hysteresis via charge control. Also methods have been developed to compensate for the non-linearity of hysteresis in AFM by inverse hysteresis models (Croft, Shed, & Devasia, 2001; Merry et al., 2009).

In high accuracy metrological AFM-systems, the sample topography is estimated by directly measuring the actuator displacement $x(t)$ with high accuracy position sensors (e.g. interferometric) (Merry et al., 2009; Trumper, Hocken, Amin-Shahidi, Ljubicic, & Overcash, 2011), as shown by Fig. 2b. The high accuracy position sensors allow us to trace back the measured sample dimensions to the international length standards. The additional position sensors, however, are generally cost-intensive and therefore not found in the most commercially available AFM instruments. Moreover, the position sensors are an additional source of measurement noise, which hampers the precision of the measurement, particulary at higher imaging bandwidths.

The assumption that the actuator displacement $x(t)$ directly represents the sample topography only holds when scanning relatively slow, allowing the feedback control loop sufficient time to recover from topography variations such that the control error is almost zero: $(e(t) \approx 0 \rightarrow h(t) \approx -x(t))$. However, at higher imaging speeds the control error is not fully zero, and part of the topography information will appear in the cantilever deflection signal $d(t)$. In Salapaka, De, and Sebastian (2005) a method is presented to design a model based controller and estimator that provides an estimate of the sample topography by taking into account both the control signal $u(t)$ and the cantilever deflection signal $d(t)$, as shown in Fig. 2c. By using the cantilever deflection signal the topography estimation bandwidth is not limited by the control bandwidth. In Lee and Salapaka (2010) this method is extended to dynamic mode imaging, taking into account a linear model of the tip–sample interaction.

Improving the imaging speed of AFM has been the focus of a significant amount of research, aimed at improving the control bandwidth of the feedback loop that controls the tip–sample force, utilizing modern model-based control methods (Salapaka et al., 2005; Schitter, Stemmer, & Allgöwer, 2004), and improved mechanical design of the positioning stages (Ando et al., 2001; Fleming, Kenton, & Leang, 2010; Knebel, Amrein, Voigt, & Reichelt, 1997; Schitter et al., 2007). However, when increasing the control bandwidth in AFM imaging, also the topography estimation becomes a highly dynamical process in which the higher order dynamics of the instrument may start to influence the instruments' accuracy. An important aspect that needs to be considered in this context is that the dynamical behavior of the system may

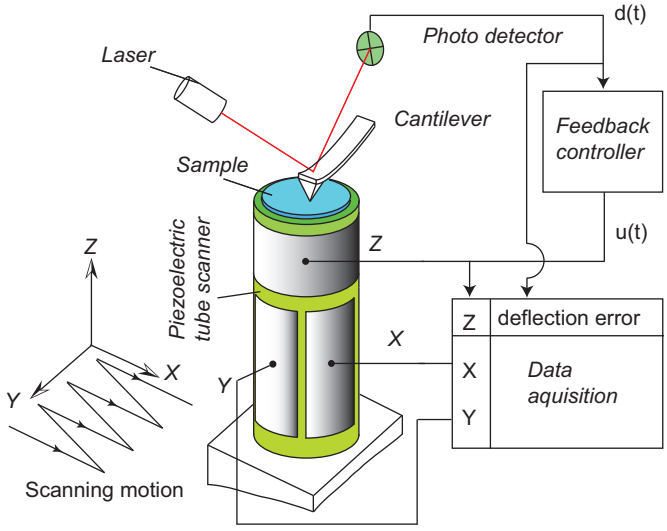

Fig. 1. Schematic of the atomic force microscope.

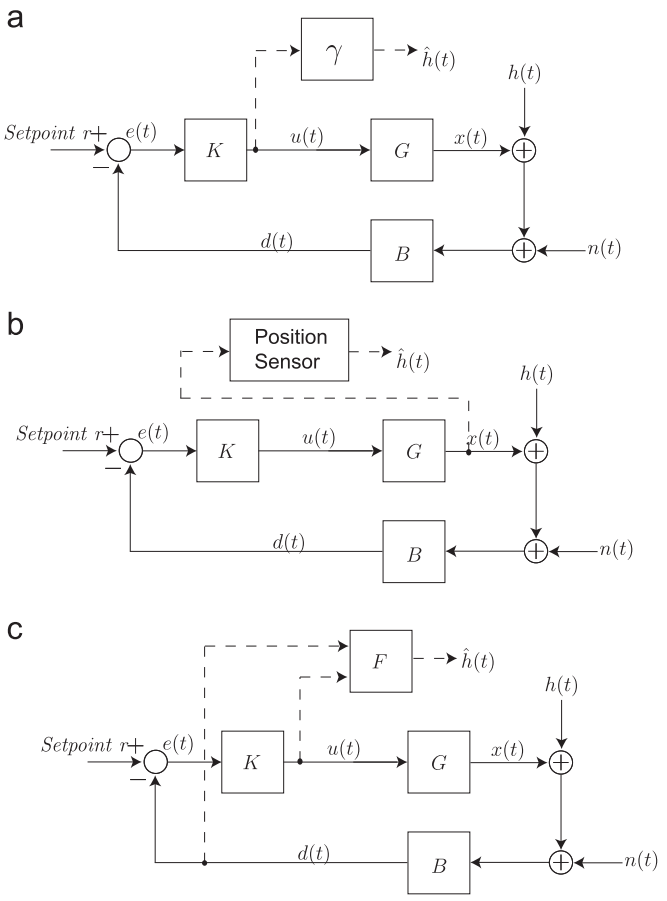

Fig. 2. Block diagrams (a–c) depict the feedback loop controlling the tip–sample force in an AFM system, with actuator dynamics G, sensor dynamics B, and feedback controller K, topography signal $h(t)$, cantilever deflection signal $d(t)$, controller output $u(t)$, actuator displacement $x(t)$, control error $e(t)$, and noise signal $n(t)$, and estimated sample topography $\hat{h}(t)$. The dashed lines in blockdiagram (a) depict the conventional methods for topography estimation based on a calibrated scaling of controller output $u(t)$. Blockdiagram (b) depicts the topography estimation as in metrological AFM, using a dedicated position sensor. Blockdiagram (c) depicts the concept of model-based topography estimation, using both the controller output $u(t)$ and the cantilever deflection signal $d(t)$ in the topography estimation.

show variations due to the varying weight and alignment of the sample and cantilever, and due to the varying imaging conditions. As these dynamical variations are largely unpredictable, these constitute a certain degree of dynamical uncertainty which limits the modeling accuracy of the system dynamics, and thus of the ability of accurately estimating the sample topography (Kuiper, Van den Hof, & Schitter, 2012). This becomes more relevant for high speed AFM applications in which the bandwidth of the system is pushed to higher frequencies, leading to stronger excitation of the higher order dynamics of the system, which typically constitute larger dynamical uncertainty.

This paper is focused on how the dynamical uncertainty of the system influences the accuracy of the topography estimate, and how this could be addressed in the design of the feedback controller and topography estimator, assuming the system topology as in Fig. 2c. In Section 2, the influence of the dynamical uncertainty on the topography estimation accuracy is analyzed. Section 3 presents an integrated design methodology for the feedback controller and topography estimator in AFM, which is demonstrated on a commercially available AFM system in Section 4. In Section 5, the influence of the dynamical uncertainty on the accuracy of the topography is experimentally verified, and conclusions are drawn in Section 6.

2. Topography estimation problem

In order to analyze the topography estimation problem in AFM, in this section the optimal topography estimator is derived based on the Wiener theory (Vaseghi, 2009). Based on the expression of the optimal topography estimator it is analyzed how the topography estimation accuracy is influenced by the dynamical uncertainty of the system and by the design of the feedback controller. While both the cantilever deflection signal $d(t)$ and the control signal $u(t)$ are available for the topography estimation, the later one can be directly derived from the first given that the feedback controller is known: $u(t)=K(p)\cdot d(t)$. Therefore without loss of generality the topography estimation problem can be posed as a filtering problem solely based on the cantilever deflection signal $d(t)$. Later on in this section the practical considerations are discussed which motivate the use of both available signals $u(t)$ and $d(t)$ for the topography estimation. Moreover, in the following analysis the setpoint is neglected as this is constant throughout each imaging experiments (i.e. $r=0$). Hence, the topography estimation problem may be depicted as in the block diagram of Fig. 3, with the system dynamics M and the topography estimator F. Assuming linear dynamics the sensor output in AFM is given as

$$d(t)=\underbrace{\frac{B(p)}{1+L(p)}}_{M(p)}\cdot(h(t)+n(t)), \tag{1}$$

with the loop gain $L(p)=G(p)\cdot K(p)\cdot B(p)$. The sensor signal $d(t)$ is the input for the sample topography estimator F which provides an estimate of the sample topography

$$\hat{h}(t)=F(p)\cdot d(t), \tag{2}$$

The topography estimation error is now given as

$$\varepsilon(t)=\hat{h}(t)-h(t)=F(p)\cdot d(t)-h(t), \tag{3}$$

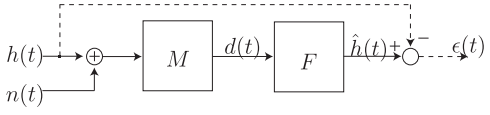

Fig. 3. Block diagram depicting the topography estimation problem in AFM as a filtering problem based on the cantilever deflection signal $d(t)$.

The mean square error value of this signal can be derived via the Parsevals theorem as

$$\mathbf{E}[\varepsilon(t)^2]=\frac{1}{2\pi}\int_{-\infty}^{\infty}\Phi_\varepsilon(\omega)\,d\omega \tag{4}$$

with $\Phi_\varepsilon(\omega)$ being the power spectral density of the topography estimation error signal, which is given as

$$\Phi_\varepsilon(s)=F(s)\cdot F^*(-s)\cdot\Phi_d(s)-F(s)\cdot\Phi_{dh}(s)-F^*(-s)\cdot\Phi_{hd}(s)+\Phi_h(s). \tag{5}$$

By setting the derivative of $\Phi_\varepsilon(s)$ with respect to the estimator filter $F(s)$ to zero the following expression for the optimal Wiener filter can be obtained (Vaseghi, 2009)

$$F(s)=\frac{\Phi_{hd}(s)}{\Phi_d(s)}=\frac{M^*(-s)\Phi_h(s)}{M(s)M^*(-s)(\Phi_h(s)+\Phi_n(s))}=\underbrace{\frac{\Phi_h(s)}{\Phi_h(s)+\Phi_n(s)}}_{F_2(s)}\cdot\underbrace{\frac{1}{M(s)}}_{F_1(s)}, \tag{6}$$

in which the fact is used that the topography signal $h(t)$ and the noise signal $n(t)$ are not correlated. As shown by Eq. (6) the optimal estimator can be split in a part that handles the noise denoted F_2, and a part that inverts the system dynamics denoted F_1. Notice that the design of filter F_2 influences the precision of the topography estimation by handling the random noise. Filter F_1 is responsible for proper scaling of the measurement signals at different frequencies, which strongly determines the accuracy of the topography estimation.

The spectrum of $h(t)$ is depending on the sample topography profile and the imaging speed, of which the first is not known beforehand and varies strongly between different experiments. Therefore, by splitting the design of the estimator, the part inverting the system dynamics F_1 needs to be designed only once, while the noise filter F_2 can be adjusted for the changing imaging conditions. The design and application of F_2 to filter out the measurement noise can be done after the imaging data is obtained and analyzed. Such filtering of the imaging data to filter out the (high frequency) noise is a common procedure during the post-processing of the AFM images (Easton & West, 2010).

From Eqs. (1) and (6) the estimated sample topography based on the optimal Wiener filter can be written as

$$\begin{aligned}\hat{h}(t)&=F_2(p)\cdot F_1(p)\cdot d(t)=F_2(p)\cdot\frac{1}{M(p)}\cdot d(t),\\&=F_2(p)\cdot[\hat{B}^{-1}(p)+\hat{G}(p)\cdot K(p)]\cdot d(t),\\&=F_2(p)\cdot[\hat{B}^{-1}(p)\ \ -\hat{G}(p)]\cdot\begin{bmatrix}1\\-K(p)\end{bmatrix}\cdot d(t),\\&=F_2(p)\cdot\underbrace{[\hat{B}^{-1}(p)\ \ -\hat{G}(p)]}_{\tilde{F}_1}\cdot\begin{bmatrix}d(t)\\u(t)\end{bmatrix},\end{aligned} \tag{7}$$

with $\hat{G}$ and $\hat{B}$ being the models of the actuator and sensor dynamics, respectively (the $\hat{\ }$ is used here to distinguished the estimated transfer functions from the true transfer functions). The resulting topography estimator is in the form as shown in Fig. 2c. Eq. (7) shows that by taking the output of the feedback controller $u(t)$ into account in the topography estimate (as is also done in conventional AFM) the dynamics of the feedback K do not need to be taken into account in the topography estimator, which simplifies the design of the estimator. However, the resulting topography estimator does require dynamical models of the sensor dynamics $\hat{B}$ and of the actuator dynamics $\hat{G}$ in order to accurately represent the sample features, as shown by Eq. (7).

In dynamic mode AFM, the cantilever dynamics in B are nonlinear, making it difficult to model. Therefore, in dynamic mode AFM one strongly relies on the controller output $u(t)$ for estimation of the sample topography, presuming a good linearization effect of the feedback loop. Recently, however, techniques are

developed to explicitly handle the cantilever dynamics in dynamic mode AFM (Jeong, Jayanth, Jhiang, & Menq, 2006; Lee & Salapaka, 2010; Sahoo, Sebastian, & Salapaka, 2003). In contrast, for contact-mode AFM the cantilever dynamics can be regarded fairly linear (Schitter et al., 2001), and calibration of the sensor gain in B can be done before each imaging experiment by performing a force curve measurement (Sarid, 1994).

The modeling of the higher order actuator dynamics in $\hat{G}$ is neglected in conventional AFM-systems and the actuator displacement is approximated by a static scaling of the control signal $u(t)$, i.e. the actuator model $\hat{G}$ is taken as static. In high-speed AFM-systems, however, the bandwidth of the feedback loop is pushed close to, or even beyond the first the resonance frequency of the actuator, such that a dynamical actuator model $\hat{G}$ must be used for more accurate sample topography estimation (Salapaka et al., 2005; Schitter et al., 2001).

Notice that when the noise $n(t)$ is assumed to be zero, the noise filter of Eq. (6) becomes $F_2=1$, and the transfer from the topography signal $h(t)$ towards the topography estimation error $\varepsilon(t)$ can be calculated as

$$F_1(p)\cdot M(p)-1=\frac{\hat{B}^{-1}(p)B(p)+\hat{G}(p)\cdot K(p)\cdot B(p)}{1+L(p)}-1,$$

$$=\frac{[\hat{B}^{-1}(p)B(p)-1]+[\hat{G}(p)-G(p)]\cdot K(p)\cdot B(p)}{1+L(p)}, \qquad (8)$$

i.e. part of the topography estimation error is stemming from the modeling error of the sensor dynamics $[B(p)\cdot\hat{B}^{-1}(p)-1]$, and partly from the modeling error of the actuator dynamics $[\hat{G}(p)-G(p)]$. Hence, the accuracy of the topography estimation is strongly depending on the accuracy of the models for the sensor dynamics, and of the actuator dynamics.

The accuracy of the dynamical models may be hampered by variations in the dynamical behavior of the system, caused for instance by changing the cantilever, the sample mass, or the alignment of the sample on the scanner (van Hulzen, Schitter, Van den Hof, & van Eijk, 2012). While during each AFM imaging experiment the system dynamics may be largely constant, the dynamical variations mostly occur from one imaging experiment to the next when setting up the new experiment. Although it is possible to identify these dynamical variations before each imaging experiment, this is not desirable as such identification experiments are time-consuming, require special expertise of the operator, and may cause damage of the tip or the sample. Therefore, the dynamical variations of the system constitute a certain degree of dynamical uncertainty, which limits the modeling accuracy of the system dynamics, and therefore poses a limitation on the accuracy of the topography estimation.

Important is to note the influence of the feedback controller K in Eq. (8), which determines the propagation of the modeling errors towards the topography estimation error. Hence, due to the inevitable modeling errors of the system dynamics, the feedback control problem and the topography estimation problem are coupled. Consequently, the design of the feedback controller should be done not only considering the requirements on the control of the tip–sample force, but also considering the influence of the feedback controller on the accuracy of the topography estimation. Therefore, in the next section an integrated design methodology is proposed to handle this combined control and estimation problem in AFM, while in Sections 4 and 5 the coupling between the control and estimation problems is experimentally verified based on a commercially available AFM system.

3. Robust design of the feedback controller and the topography estimator

The feedback controller and topography estimator should be designed such that (i) sufficiently fast tracking of the sample profile is provided in order to prevent too high force variations between the tip and the sample, which might cause damage of the tip or sample, and (ii) the topography estimation error can be guaranteed to be within certain specifications, given the dynamical uncertainty of the system. As discussed in the previous section, the feedback control problem and the topography estimation problem are coupled due to the dynamical uncertainty of the system. To handle this coupled control and estimation problem in AFM the $\mathcal{H}_\infty$ framework (Skogestad & Postlethwaite, 2005) is well suited as it allows to synthesize the controller and the estimator to guarantee certain specifications on the system performance taking into account the dynamical uncertainty of the system. Therefore, in this research an integrated design methodology is proposed to design the feedback controller and topography estimator based on robust $\mathcal{H}_\infty$ control techniques.

For simplicity, in the following only contact-mode imaging is considered in which the sensor dynamics B are assumed to be fully known, static, and normalized, i.e. $(B=\hat{B}=1)$. However, most of the considerations also hold for dynamic mode AFM. This section is focused on the part of the topography estimator that inverts the systems dynamics, denoted F_1 in Eq. (6), as this part is responsible of the accuracy of the topography estimate. The influence of measurement noise is neglected in this section (i.e. $F_2=1$).The proposed design methodology consists of three steps:

1. The first step in the design process is to identify the dynamical behavior of the system, including its dynamical variations, and to capture this dynamical behavior within a parametric model that can be used for model-based design of the feedback controller and the topography estimator.
2. In a second step the feedback controller and topography estimator are designed via μ−synthesis (Skogestad & Postlethwaite, 2005) to satisfy certain specifications on the system performance, given the system dynamics captured by the model.
3. In contrast to the feedback controller, the topography estimator is not required to run in realtime which allows a higher computational complexity, and therefore allows the use of higher order dynamical models which may yield a better accuracy of the topography estimate. Therefore, in a third step the design of the estimator is improved by obtaining higher order models of the system dynamics, taking into account the dynamics of the designed feedback controller.

In the subsequent sections these steps of the proposed design method are discussed in more detail.

3.1. Step 1: identification and modeling of the actuator dynamics

The dynamics of the z-actuator in AFM can be identified by driving the actuator with an excitation signal and measuring the cantilever deflection signal, while the lateral scanning motion is disabled. When using cantilevers with resonance frequencies higher than the frequency range of interest, while using small enough excitation amplitudes to keep the tip in firm contact with the sample during the identification experiments, the cantilever dynamics can be regarded as static and their influence can be neglected within these experiments. In order to identify the dynamical behavior of the system, including its uncertainty under all working conditions, the measurements are repeated with different sample discs and by changing the alignment of the

sample disc on the scanner. The recorded frequency responses are denoted $\Upsilon_j(\omega_f)$, with $j\in[1\ldots k]$ being the jth frequency response measurement and k the number of different frequency response measurements. The various load conditions during the identification experiments should be chosen such that the set of frequency responses $\Upsilon_j(\omega_f)$ gives a good and complete resemblance of how the system is used in practice. Based on the frequency response measurements of $\Upsilon_j(\omega_f)$ a nominal model and the corresponding dynamical uncertainty set can be fitted that captures the dynamical behavior of the system with all possible combinations of measurement probes and samples

$$\breve{G}(s,\Delta) = G_n(s)\cdot(1+\Delta(s)\cdot Q(s)) \tag{9}$$

$$\mathcal{G}(s) = \{\breve{G}(s,\Delta), \|\Delta(s)\|_\infty \le 1\}, \tag{10}$$

with $G_n(s)$ being a parametric model of the nominal actuator dynamics, and filter $Q(s)$ and uncertain parameter $\Delta(s)$ capturing the dynamical variations of the system. To minimize the conservatism of the model the nominal model $G_n(s)$ can be obtained by first determining the optimal non-parametric response of the nominal model at each frequency point which minimizes the worst-case modeling error

$$\Gamma(\omega_f) = \alpha(\omega_f) + i\cdot\beta(\omega_f), \tag{11}$$

$$\{\alpha(\omega_f),\beta(\omega_f)\} = \arg\min_{\alpha(\omega_f),\beta(\omega_f)} \max_{j=1\ldots k} |\Upsilon_j(\omega_f) - \alpha(\omega_f) - i\cdot\beta(\omega_f)|. \tag{12}$$

The minimization of Eq. (12) has to be solved as an optimization problem at each frequency point, similar as described in de Callafon, Nagamune, and Horowitz (2006). Based on the optimal nonparametric nominal response $\Gamma(\omega_f)$, a parameterized nominal model $G_n(s)$ can be obtained by data fitting techniques (Pintelon & Schoukens, 2001). Given the parametric nominal model $G_n(s)$ and the identification data from the various measurement trials, the worst-case multiplicative modeling error can be determined at each frequency point

$$\Psi(\omega_f) = \max_{j=1\ldots k} \left| \frac{\Upsilon_j(\omega_f) - G_n(\omega_f)}{G_n(\omega_f)} \right|. \tag{13}$$

The maximum multiplicative modeling error $\Psi(\omega_f)$ can be incorporated in the set of Eq. (9), via a parameterized over-bounding function $Q(\omega_f)\ge\Psi(\omega_f)$. The overbounding filter $Q(s)$ can be obtained using spectral overbounding techniques (Kinney, de Callafon, & de Oliveira, 2007; Scheid & Bayard, 1995).

3.2. Step 2: model-based feedback controller and estimator design

Based on the dynamical model of Eq. (9), the feedback controller and topography estimator are designed to guarantee $\mathcal{H}_\infty$–norm bounded performance specifications on the control error, and the topography estimation error. Therefore, the design problem is cast into the mixed-sensitivity framework (Skogestad & Postlethwaite, 2005), as depicted in Fig. 4. The feedback controller

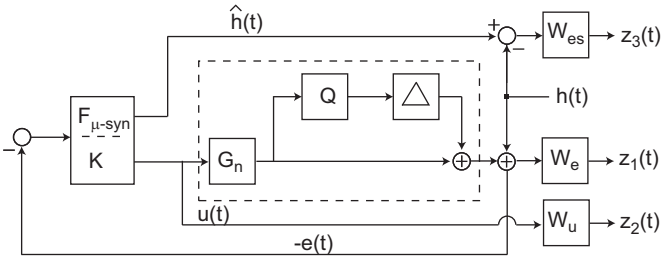

Fig. 4. System description for design of the robust feedback control and topography estimator, with input $h(t)$, and performance channel-outputs $z_1(t)$, $z_2(t)$ and $z_3(t)$. This system is the entry for the μ–synthesis of Eq. (14).

K and topography estimator $F_{\mu\text{-}syn}$ are part of the same filter which depends on the parameters θ to be found. Hence, this filter has the negative cantilever deflection signal $-d(t)$ as input, and the control signal $u(t)$ and estimated sample topography $\hat{h}(t)$ as outputs. The resulting topography estimator is in the form of Eq. (2), with only the cantilever deflection signal as input. The underscore ($_{\mu\text{-}syn}$) for the topography estimator in Fig. 4 is used to denote that this the estimator to be obtained via μ–synthesis, as also a higher order estimator design is discussed in Section 3.3. Filters $W_{es}(s)$, $W_e(s)$, and $W_u(s)$ in Fig. 4 are the weighting filters on the topography estimation error $\epsilon(t)$, the control error $e(t)$, and the controller output $u(t)$, respectively. These weighting filters can be chosen to represent the performance specification on the closed loop system, as demonstrated for a practical system in Section 4.1. This design methodology is similar as described for a nominal feedback controller and estimator design in Salapaka et al. (2005), except for the fact that here the dynamical uncertainty of the system is explicitly addressed. The objective of the controller and estimator synthesis is now formulated as to find the parameters $\bar{\theta}$ that minimize the worst-case $\mathcal{H}_\infty$–norm of the system

$$\gamma \ge \min_{\theta} \max_{\Delta} \left\| \begin{matrix} W_e(s)\cdot S(s,\theta,\Delta) \\ W_u(s)\cdot K(s,\theta)\cdot S(s,\theta,\Delta) \\ W_{es}\cdot[F_{\mu\text{-}syn}(s,\theta)\cdot S(s,\theta,\Delta) - 1] \end{matrix} \right\|_\infty, \tag{14}$$

with upper-bound γ, and the sensitivity function of the uncertain system $S(s,\theta,\Delta) = [1 +_{\breve{}} G(s,\Delta)\cdot K(s,\theta)]^{-1}$. The minimization of Eq. (14) is a non-convex optimization problem and requires iterative procedures as the μ–synthesis *DK*-iteration method (Skogestad & Postlethwaite, 2005), in order to approximate the optimal controller parameters. After controller synthesis, the robust performance of the controlled system can be analyzed in a more accurate manner based on the nonparametric frequency responses $\Upsilon_j(\omega_f)$ obtained during the identification experiments, as discussed in Section 4.3.

3.3. Step 3: improved estimator design

The topography estimator should be designed to minimize the worst case topography estimation error given the dynamical uncertainty of the system. Although for the model-based design of the feedback controller K and the topography estimator $F_{\mu\text{-}syn}$ the model of Eq. (9) is assumed, due its limited order this model captures a larger set of frequency responses than the actual system, and therefore the obtained topography estimator may not provide the best robust performance for the actual system. Moreover, the fact that the topography estimator does not have to run in realtime allows a higher computational complexity, i.e. using a higher order topography estimator, which may yield better accuracy. The topography estimation accuracy may be improved by redesigning the topography estimator, given the feedback controller K from the μ–synthesis and the frequency responses $\Upsilon_j(\omega_f)$ obtained from the identification experiments.

Based on the feedback controller K obtained via the minimization of Eq. (14), and the identified frequency responses $\Upsilon_j(\omega_f)$, the worst case magnitude of the transfer from topography signal $h(t)$ towards the topography estimation error $\varepsilon(t)$ can be determined at each frequency point by

$$\max_{j=1\ldots k} \left| \frac{\tilde{F}(\omega_f)\cdot\begin{bmatrix}1\\ -K(\omega_f)\end{bmatrix}\cdot B}{1+\Upsilon_j(\omega_f)\cdot K(\omega_f)\cdot B} - 1 \right|, \tag{15}$$

with $\tilde{F}(\omega) = [\hat{B}^{-1} \;\; -\hat{G}(\omega)]$ being the topography estimator following the structure of Eq. (7), with both the cantilever deflection signal $d(t)$, and the control signal $u(t)$ as inputs (cf. Fig. 2c), and assuming the noise filter $F_2 = 1$. While the topography estimator obtained

from the $\mu-$synthesis $F_{\mu\text{-}syn}$ is in the form of Eq. (2) with only the cantilever deflection signal as input, it can also be casted in the form of Eq. (7) by $\hat{F}_{\mu\text{-}syn}(\omega)=[\hat{B}^{-1} \quad -\hat{G}_{\mu\text{-}syn}(\omega)]$, with $\hat{G}_{\mu\text{-}syn}=(F_{\mu\text{-}syn}(\omega)-1)/K(\omega)$. Recall from Section 2 that the topography estimator with both the cantilever deflection signal $d(t)$ and the control signal $u(t)$ as inputs does not require accurate knowledge of dynamics of the feedback controller K, and therefore would yield better accuracy in practice. Assuming the sensor dynamics to be known $\hat{B}=B=1$, the worst case magnitude of the transfer from topography signal $h(t)$ towards the topography estimation error $\epsilon(t)$ of Eq. (15) becomes

$$\max_{j=1\ldots k}\left|\frac{[\hat{B}^{-1}\cdot B+\hat{G}(\omega_f)\cdot K(\omega_f)\cdot B]-[1+\Upsilon_j(\omega_f)\cdot K(\omega_f)\cdot B]}{1+\Upsilon_j(\omega_f)\cdot K(\omega_f)\cdot B}\right|,$$
$$=\max_{j=1\ldots k}\left|\frac{[\hat{G}(\omega_f)-\Upsilon_j(\omega_f)]\cdot K(\omega_f)}{1+\Upsilon_j(\omega_f)\cdot K(\omega_f)}\right|, \tag{16}$$

with $\hat{G}(\omega_f)$ being the model of the actuator dynamics within the topography estimator. Hence, based on the frequency responses of $\Upsilon_j(\omega_f)$, the optimal nonparametric topography estimator which minimizes the worst-case magnitude of the transfer from topography signal $h(t)$ towards the topography estimation error $\epsilon(t)$ at each frequency point can be found by

$$\tilde{F}_{nonpar}(\omega_f)=[\hat{B}^{-1} \quad -\hat{G}_{nonpar}(\omega_f)],$$

$$\hat{G}_{nonpar}(\omega_f)=\overline{\alpha}(\omega_f)+i\cdot\overline{\beta}(\omega_f),$$

$$\{\overline{\alpha}(\omega_f),\overline{\beta}(\omega_f)\}=\arg\min_{\alpha(\omega_f),\beta(\omega_f)}\max_{j=1\ldots k}\left|\frac{[\overline{\alpha}(\omega_f)+i\cdot\overline{\beta}(\omega_f)-\Upsilon_j(\omega_f)]\cdot K(\omega_f)}{1+K(\omega_f)\cdot\Upsilon_j(\omega_f)}\right|, \tag{17}$$

which can be calculated as a linear optimization problem at each frequency point. For practical implementation however, a parametric topography estimator is required which can be obtained from the optimal nonparametric topography estimator of Eq. (17) via least squares data fitting techniques

$$\tilde{F}_{par}(\omega_f)=[\hat{B}^{-1} \quad -\hat{G}_{par}(\omega_f)], \tag{18}$$

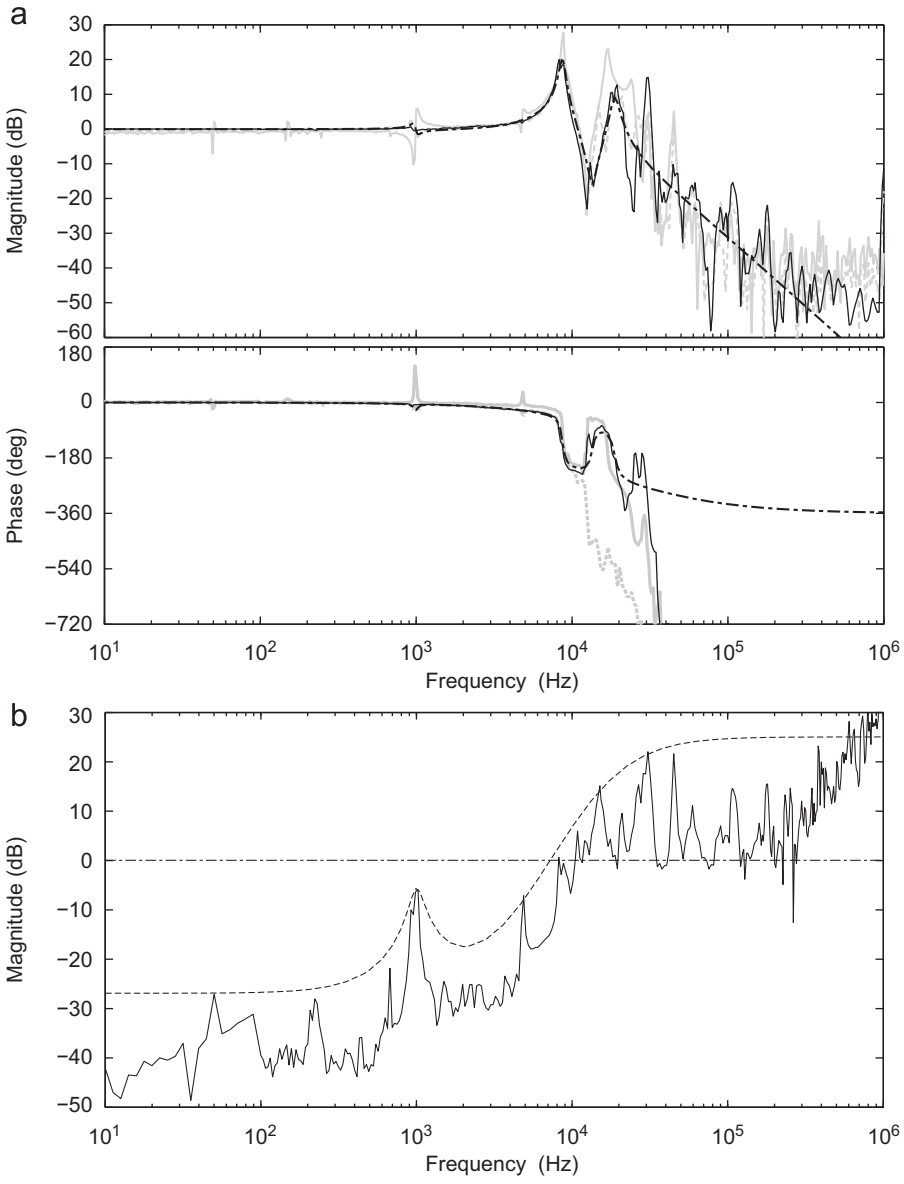

Fig. 5. (a) Frequency response of the tube scanner measured in two identification experiments (solid gray and dashed gray), the un-parameterized nominal response $\Gamma(\omega_f)$ (solid, black) calculated following Eq. (11), and the frequency response of the seventh order model $G_n(s)$ (dashed–dotted, black). (b) Bode magnitude response of the maximum multiplicative model error $\Psi(\omega_f)$ calculated according to Eq. (13), and the over-bounding filter $Q(s)$ (black, dashed).

$$\hat{G}_{par}(\omega,\overline{\varphi}) = \arg\min_{\varphi} \sum_{\omega_f=\omega_1}^{N} [\hat{G}_{par}(\omega,\varphi) - \hat{G}_{nonpar}(\omega_f)]^2. \quad (19)$$

Minimization of Eq. (19) can be done by the Sanathanan-and-Koerner method (Pintelon & Schoukens, 2001), or by instrumental variable based linear regression methods (Blom & Van den Hof, 2010).

As demonstrated in Section 4, redesigning the topography estimator with high order dynamical models significantly improves the accuracy of the topography estimate as compared to the estimator $F_{\mu-syn}$ obtained via the minimization of Eq. (14).

4. Design example and analysis

In order to verify the integrated design of the feedback controller and topography estimator presented in Section 3, the design methodology is demonstrated on the Multimode V system equipped with the J-scanner. Two different design cases are discussed and compared with different emphasis on the accuracy of the topography estimate.

4.1. Identification and modeling

In order to identify the dynamical behavior of the system and its variations, the system is setup several times with different sample discs, and by varying the alignment of the sample discs on the actuator. The actuator responses are measured by using a network analyzer (4395A, Agilent, Santa Clara, CA, USA). The system is prepared several times using different sample discs with masses ranging from 0.5 to 1 g, and by varying the alignment of the sample disc on the actuator. By only using cantilevers with high free resonance frequencies ($f_o \geq 300$ kHz) in contact mode, the sensor dynamics can be considered static below 100 kHz, which is the frequency range of interest. Therefore, the sensor dynamics B are neglected in the following analysis, and for convenience the DC-gain from actuator input $u(t)$ to cantilever deflection signal $d(t)$ is normalized ($\lim_{\omega\to 0} G(\omega)\cdot B(\omega) = 1$) in the following discussion.

The results of two different frequency response measurements are depicted in Fig. 5a, showing the first longitudinal resonance of the piezoelectric tube scanner at 8 kHz. Based on 12 different frequency response measurements, the un-parameterized nominal frequency response $\Gamma(\omega_f)$ (cf. Eq. (11)) is obtained via a linear optimization at each frequency point implemented via the optimization toolbox of `matlab`, as shown by the black solid line of Fig. 5a. The un-parameterized nominal frequency response $\Gamma(\omega_f)$ is used to fit a seventh order dynamical model $G_n(s)$ by the Sanathanan-and-Koerner method via the `fitfrd` command of `matlab`. The nominal actuator model $G_n(s)$ is shown by the dashed–dotted lines of Fig. 5a.

Based on the nominal model $G_n(s)$ the maximum multiplicative modeling error $\Psi(\omega_f)$ is determined (cf. Eq. (13)), which is shown by the solid line of Fig. 5b. The maximum multiplicative uncertainty $\Psi(\omega_f)$ clearly shows the variations in the dynamical behavior associated with the different load conditions, which tends to become larger with increasing frequency. Moreover, Fig. 5b reveals a large peak in the dynamical uncertainty at 1 kHz, which is stemming from the coupling with the first lateral resonance modes of the scanner in the x- and y-directions. The dynamical uncertainty shown in Fig. 5b poses a strong limitation on the achievable control bandwidth, and on the accuracy of the topography estimate. In order to incorporate this dynamical uncertainty into the model of Eq. (9), a fifth order over-bounding function $Q(s) \geq \Psi(\omega_f)$ is obtained by the via the log-Chebychev algorithm based `fitmagfrd` command of `matlab`, and manually adjusted to provide a tight over-bound for the dynamical uncertainty, as is shown by the dashed line of Fig. 5b.

While the frequency response measurements discussed above are captured with small amplitude excitation signals, for larger signals these type of piezoelectric actuators may suffer from hysteresis. For this particular actuator the hysteresis is measured to cause a gain variation of less then 1.5% at full positioning range (Kuiper et al., 2012). These gain variations are, however, significantly smaller than the dynamical uncertainty stemming from the varying load conditions. Therefore, the 1.5%, or −36 dB dynamical uncertainty stemming from the hysteresis is considered to be sufficiently captured by the dynamical overbounding function $Q(s)$. For AFM systems with more severe actuator hysteresis, a method is presented in Kuiper et al. (2012) to explicitly address the hysteresis in the topography estimation utilizing a charge measurement.

4.2. Controller and estimator design

The dynamical model obtained from the identification experiments is used for the design of the feedback controller K and topography estimator $F_{\mu-syn}$ following the $\mu-$synthesis procedure as discussed in Section 3.2. To enforce the desired disturbance rejection characteristics of the closed-loop system, the weighting filter $W_e(s)$ (cf. Fig. 4) is shaped as an inverse high-pass filter. The weighting filter $W_u(s)$ on the controller output is shaped as an inverse high-pass filter with a corner frequency of 6 kHz enforcing a high frequency roll-off to attenuate high frequency noise and higher order dynamical modes of the system. The emphasis which is given on the accuracy of the topography estimation can be tuned via the weight $W_{es}(s)$. In order to analyze the consequences of taking the topography estimation problem directly into account when designing the feedback controller, two different feedback controllers and corresponding topography estimators are synthesized, using different weights on the topography estimation error: $W_{es}(s) = 1$, and $W_{es}(s) = 8$. With these static weights the topography estimation error is weighted evenly strong over all frequencies, while also frequency depended weights on the topography estimation error may be used. Given these weights on the topography estimation error, the cornering bandwidth of the weighting filter on the control error $W_e(s)$ is tuned up to the point

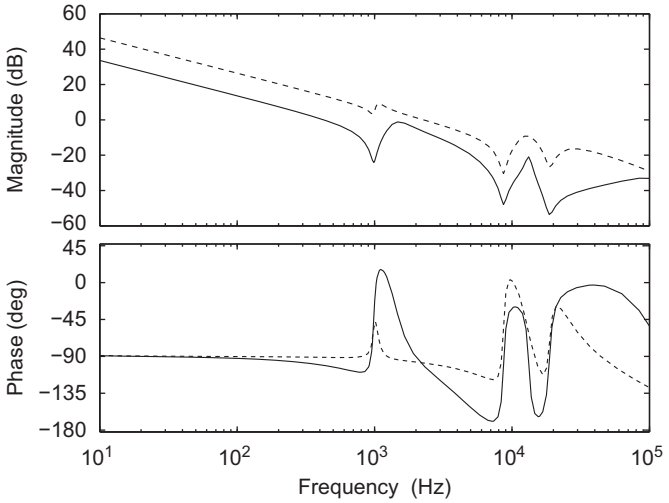

Fig. 6. Open-loop frequency response plots of the designed feedback controllers. The dashed lines correspond to the design case with lower emphasis on the topography estimation accuracy ($W_{es} = 1$), and the solid lines correspond to the design case with higher emphasis on the topography estimation accuracy ($W_{es} = 8$).

that the synthesis objective $\gamma \leq 1$ (cf. Eq. (14)) is just met. This allows one to find the maximum control bandwidth of the system given the performance specification on the topography estimation accuracy. After the $\mu-$synthesis, for both design cases a 30th order parametric topography estimator F_{par} is designed according to the procedure discussed in Section 3.3.

4.3. Performance analysis

Fig. 6 shows the open-loop frequency response plots of the feedback controllers corresponding to both design cases. Notice that in the design case with higher emphasis on the topography estimation accuracy (solid lines, Fig. 6) a lower overall controller gain is obtained, as well as a steep notch filter at 1 kHz that suppresses the dynamical uncertainties associated with the lateral resonance of the tube-scanner in that frequency region (cf. Fig. 5b). Fig. 7 shows the Bode magnitude plots of the nominal sensitivity function and the nominal complementary sensitivity function for both design cases, showing that both the disturbance rejection bandwidth (400 Hz vs. 1 kHz) and the tracking bandwidth (600 Hz vs. 3 kHz) are significantly lower for the design case with higher emphasis on the topography estimation accuracy.

Fig. 8 shows the worst-case magnitude of the transfer form topography signal $h(t)$ towards the topography estimation error $\epsilon(t)$ according to Eq. (15), analyzed for both design cases with the topography estimator $F_{\mu\text{-}syn}$ obtained from the $\mu-$synthesis (gray lines) and with the 30th order estimator F_{par}, designed according to Eq. (18) (black lines). The solid lines, and the dashed lines in Fig. 8 correspond to the design cases $W_{es}(s)=1$, and $W_{es}(s)=8$, respectively. The magnitudes of these graphs provide a measure of the accuracy of the topography estimate at each frequency point.

Comparing the results of Figs. 7 and 8 shows that for the system with the lower control bandwidth (solid lines), the accuracy of the topography estimate is better as compared to the case with the higher control bandwidth (dashed lines), particulary at higher frequencies. This is explained by the fact that with a lower control bandwidth, also the excitation of the uncertain dynamics is lower, which improves the accuracy of the topography estimation. Hence, Figs. 7 and 8 clearly reveal the design trade-off between the control bandwidth of the system and the accuracy of the topography estimate.

Furthermore, comparing the gray lines in Fig. 8 corresponding to the cases with the topography estimator $F_{\mu\text{-}syn}$ directly stemming from the $\mu-$synthesis, with the black lines in Fig. 8 corresponding to the topography estimator F_{par} obtained according to Eq. (18), shows that for both design cases the topography estimation accuracy is significantly improved by the higher order dynamical models in F_{par}. Hence, these results clearly motivate the need for redesigning the topography estimator after the $\mu-$synthesis, as discussed in Section 3.3.

5. Experimental results

The feedback controllers and topography estimators designed in Section 4 are implemented on the physical system in order to experimentally verify three different aspects:

1. The two design cases discussed in Section 4 resulted in two feedback controllers with a different control bandwidth. In Section 5.2 the better the tracking performance of the high bandwidth feedback controller is validated.
2. While neglected in conventional AFM systems, in Section 2 it is shown that the system dynamics need to be addressed within the topography estimation in order to improve the accuracy, as also recognized in Schitter et al. (2001) and Salapaka et al. (2005). In Section 5.3 the improved accuracy is experimentally validated by comparing (i) the accuracy of a topography estimator where the actuator dynamics are neglected and a static actuator model is used (i.e. $\hat{G}=c$), and (ii) the accuracy of

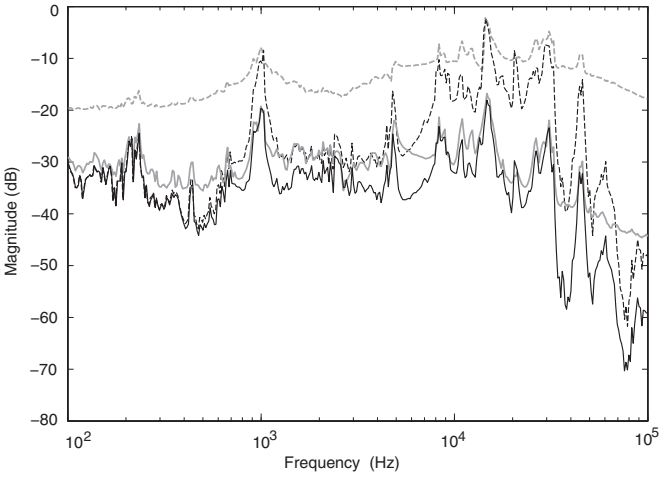

Fig. 8. Worst-case magnitude of the transfer from topography signal $h(t)$ towards the topography estimation error $\epsilon(t)$ according to Eq. (15), determined at each frequency point for the closed-loop system designed with $W_{es}=1$ (dashed lines), and $W_{es}=8$ (solid lines). The gray lines correspond to the systems with the topography estimator $F_{\mu\text{-}syn}$ directly obtained from the $\mu-$synthesis, while the black lines correspond to the systems with the 30th order parametric estimator F_{par} according to Eq. (18).

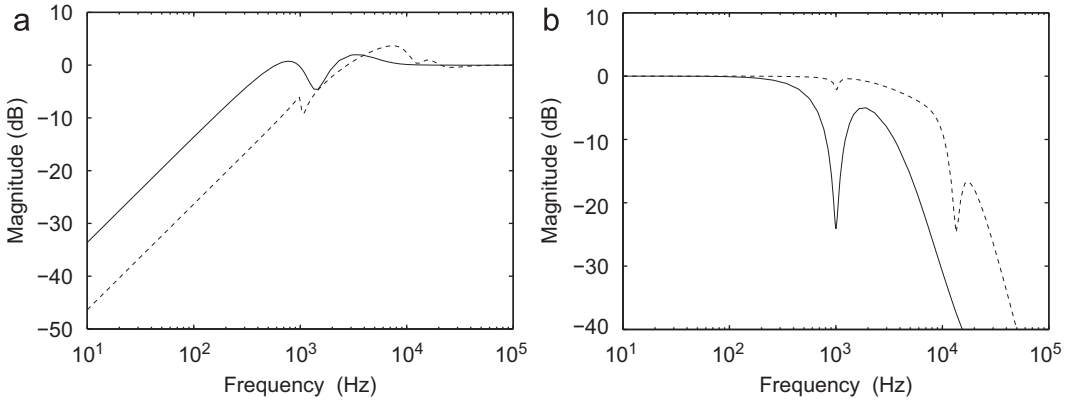

Fig. 7. Frequency response plot of the nominal sensitivity function (a) and the nominal complementary sensitivity function (b). The dashed lines correspond to the design case with lower emphasis on the topography estimation accuracy ($W_{es}=1$), and the solid lines correspond to the design case with higher emphasis on the topography estimation accuracy ($W_{es}=8$).

a topography estimator which includes a dynamical actuator model $\hat{G}_{par}(s)$ designed according to Eq. (18).

3. In Section 2 it is shown that due to the dynamical uncertainty of the system, the feedback control problem and the topography estimation problem are coupled. In Section 4, it is shown that due to this coupling a trade-off has to be made between the control bandwidth and the accuracy of the topography estimate. In Section 5.4 this trade-off is experimentally validated.

5.1. Implementation

The feedback controllers are implemented on the AFM system using a *Field-Programmable-Gate-Array* (FPGA, Virtex-II Pro Xtreme-DSP Development Kit, Nallatech, Camarillo, CA, USA). To facilitate the implementation the 21st order low-bandwidth controller and the 25th order high-bandwidth controller obtained from the $\mu-$synthesis are order reduced via the balanced truncation method (Skogestad & Postlethwaite, 2005) to 8th and 10th order, respectively. The controllers are discretized to a sampling rate of 260 kHz, and implemented on the *FPGA* in a biquad structure. The computation of the (model-based) topography estimation is done offline, by recording the cantilever deflection signal and the control signal via the data acquisition channels of the Nanoscope V controller, and filtering the data with the designed estimator in `Simulink` of `matlab`.

In order to isolate the topography estimation errors stemming from the dynamical uncertainty of the system from other error sources such as a potential scanner drift in the lateral plane and the finite sharpness of the tip, an artificial topography signal is added to the sensor signal using an analog summing amplifier, while the scanning motion of the system is disabled. As the artificial topography signal is fully known, this method allows one to accurately verify the topography estimation errors stemming from the dynamical uncertainty of the system.

To compare the system performance with the different feedback controllers and topography estimators, a 200 Hz blockwave signal with an amplitude of 250 nm is applied to the system as 'topography' signal and the system responses are measured, as shown in Fig. 9. The resulting signals are captured at a sampling rate of 100 kHz, of which the time stamp is denoted t_k, with $k\in[0,\ldots,m]$ the recorded data samples. In order to judge the consistency of the results, these experiments are repeated three

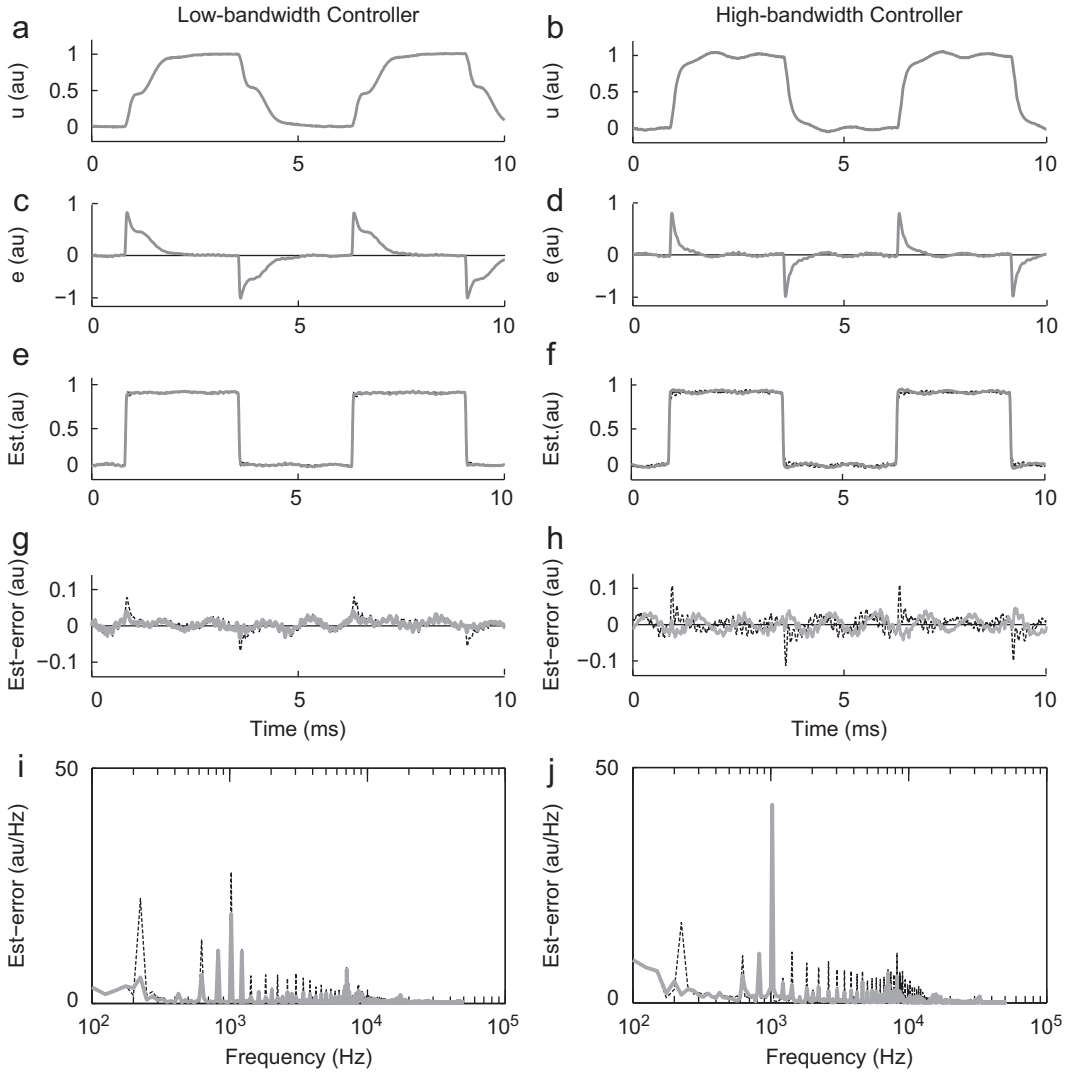

Fig. 9. AFM signals when applying a 200 Hz, 250 nm block wave signal as an artificial topography signal, for the case with the low bandwidth controller (a, c, e, g, i), and for the case with the high bandwidth controller (b, d, f, h, j). (a) and (b) shows the applied topography signal together with the output of the feedback controller, while (c) and (d) shows the control error. (e) and (f) shows the outputs of the topography estimator, while (g) and (f) shows the topography estimation error, and (i) and (j) shows the frequency spectra of the topography estimation error signal. The black dashed lines in (e) and (j) correspond to the case when using a static actuator model in the topography estimator, and the gray solid lines correspond to the case when using the dynamic actuator model in the topography estimator.

Table 1
Tracking error and topography estimation error in (nm) when applying a 200 Hz, 250 nm amplitude blockwave signal as topography signal to the system with the two designed feedback controllers and topography estimators; obtained in different but typical experiments (a, b, c) with varying load conditions on the scanner.

		400 Hz controller			1 kHz controller		
Experiment series		a	b	c	a	b	c
Tracking error	e_{RMS} (nm)	75	80	65	48	43	50
Topography estimation error							
Static	ε_{RMS} (nm)	5	5	4	6	6	7
actuator model	ε_{max} (nm)	23	23	25	33	43	33
Dynamic	ε_{RMS} (nm)	3	3	3	5	7	6
actuator model	ε_{max} (nm)	15	13	10	25	23	23

times while varying the weight and alignment of the sample on the scanner, of which the results are listed in Table 1. The results depicted in Fig. 9 correspond to the experiment series denoted 'a' in Table 1.

Notice that the magnitudes of the control errors and the topography estimation errors of the different experiments listed in Table 1 strongly depend on the amplitude and frequency content of the applied topography signal. However, the chosen block-wave signal contains many different frequency components such that the obtained results are representative for a broad range of imaging experiments.

5.2. Tracking performance

Fig. 9a and b shows the controller outputs $u(t_k)$ (solid lines) for the system with the low-bandwidth and with the high bandwidth controller captured from one experiment, along with the applied reference signal (dashed-lines). Fig. 9c and d shows the corresponding measured tracking errors. Fig. 9a and d clearly reveals that the system controlled by the high bandwidth controller provides faster recovery of the changes in sample profile. The results of the various experiments listed in Table 1 show that the RMS value of the tracking error $\left(e_{RMS}=\sqrt{(1/m)\sum_k^m e^2(t_k)}\right)$ is about 30% lower in case of the high bandwidth feedback controller. The smaller tracking errors imply lower tip–sample force variations when imaging, which result in more gentle probing of the sample matter and less chances of damaging the tip or sample.

5.3. Influence of the estimator order on the topography estimation accuracy

Based on the recorded controller output $u(t_k)$ and the cantilever deflection signal $d(t_k)$, the topography signal is reconstructed using the topography estimator (cf. Eq. (7)), which is implemented in `Matlab-Simulink`. Fig. 9e and f shows the estimated topography signals $\hat{h}(t_k)$ stemming from the topography estimators in two cases: (i) a topography estimator using a static actuator model $\hat{G}=c$ (black dashed lines), as is done in conventional AFM systems, and (ii) a topography estimator with the 30th order dynamical actuator model $\hat{G}(s)$ (gray solid lines) designed according to the procedure discussed in Section 3.3. This dynamical model is discretized by a bilinear transformation (Tustin method) to the sampling rate of 100 kHz via the `c2d.m` command of `matlab`. Hence, the sample topography is obtained as $\hat{h}(t_k)=e(t_k)-\hat{G}(p_k)\cdot u(t_k)$ for the dynamical actuator model, or $\hat{h}(t_k)=e(t_k)-c\cdot u(t_k)$ for the static actuator model, as respectively shown by the solid gray and dashed black lines in Fig. 9e and f. The topography estimation errors $\varepsilon(t_k)=\hat{h}(t_k)-h(t_k)$ are shown in Fig. 9g and h, demonstrating significantly less topography estimation error when using the dynamical actuator model in the topography estimator, especially at the representation of the sharp edges of the sample topography. Table 1 lists both the RMS $\left(\varepsilon_{RMS}=\sqrt{(1/m)\sum_k^m \epsilon^2(t_k)}\right)$ and the peak values of the topography estimation error ($\varepsilon_{max}=\max_{k\in[1,\ldots,m]}|\epsilon(t_k)|$) for the different experiments, for the systems with either the static or the dynamic actuator model. Table 1 shows that in these experiments the peak of the topography estimation error is 25% to 60% less for the system with a dynamical actuator model, both with the low and with the high bandwidth controller. In case of the low bandwidth controller, the RMS value of the topography estimation error is about 30% less for the system with dynamical actuator model. In case of the high bandwidth controller, the difference between both estimator designs in terms of the RMS value of the topography estimation error is less pronounced, which is due to the stronger excitation of the dynamical couplings with the lateral resonance mode at 1 kHz with the high bandwidth controller. The dynamical couplings with this lateral resonance mode strongly depend on the alignment of the sample disc on the scanner, and therefore causes large dynamical uncertainty at 1 kHz as also shown by Fig. 5b. Fig. 9i and j shows the frequency spectra of the topography estimation errors, clearly indicating that the system with dynamical actuator model performs better at all frequencies, apart from the frequency region of the first lateral resonance mode at 1 kHz. This is explained by the fact that the dynamic actuator model is designed to minimize the worst-case modeling error over all possible experiments (cf. Section 3.1), which does not guarantee that it provides the best match in every experiment. However, the results shown in Fig. 9e and h and Table 1 clearly reveal the overall benefit of using a dynamic actuator model in the topography estimate, especially for the representation of the sharp edges of the sample.

5.4. Influence of the controller bandwidth on the topography estimation accuracy

Comparing the topography estimation errors stemming from the system with the low bandwidth controller with those of the system with the high bandwidth controller clearly reveals that the accuracy of the topography estimate is about 40% better with the low bandwidth controller, both in terms of RMS and in peak error. Therefore, these results clearly confirm the trade-off between the bandwidth and the accuracy of the topography estimate, as also shown by the frequency domain results in Fig. 8.

The frequency spectra of the topography estimation error signals, shown in Fig. 9i and j, clearly reveal that the major frequency components of the topography estimation signals are around the lateral resonance mode at 1 kHz and at the first longitudinal resonance mode at 8 kHz, which correspond to the frequency regions with the highest dynamical uncertainty (cf. Fig. 5). Hence, these results show good resemblance with the frequency domain results obtained in Section 4.

6. Conclusions

This paper presents an integrated approach for the design of a robust feedback controller and topography estimator for AFM,

taking into account the dynamical uncertainties of the AFM-system. The proposed design approach is demonstrated on a commercially available AFM-system, showing two different designs with different emphasis on the accuracy of the topography estimation. Experimental results verify that due to the dynamical uncertainty of the instrument a trade-off has to be made between the control bandwidth of the feedback loop controlling the tip–sample force, and the accuracy of the topography estimation. Moreover, it is experimentally verified that the use of a dynamic actuator model in the sample topography estimator significantly improves the accuracy of the measured topography.

As a consequence of the trade-off between the control bandwidth and the accuracy, the intended imaging applications of the instrument should be considered when designing the feedback controller and topography estimator in AFM. When imaging for instance fragile biological samples, minimizing the force variations between the tip and the sample may be most important in order not to damage the sample, aiming for an as high as possible control bandwidth and therefore the requirements on the accuracy of the topography estimation may be relaxed. However, in other application such as quality assurance in the semiconductor industry, higher emphasis might be given on the quality of the topography estimation. Samples from material science or semiconductors potentially are not as fragile as biological systems, and higher importance may be given to the metrological aspects of the instrument. The integrated design method proposed in this contribution can be used to handle this design trade-off and adapt the feedback controller and topography estimator of the system to the particular imaging application.

These results also indicate that reducing the dynamic uncertainty of the system may be an important design criterion for future AFM development. The dynamical uncertainty may be reduced by for instance fixing the alignment of the sample on the scanner, and by normalizing the weight of the sample discs. The coupling with the lateral resonance modes of the piezoelectric tube scanner has shown to be a large source of dynamical uncertainty, which may be reduced by damping the lateral resonances by active feedback control (Kuiper & Schitter, 2010; Tamer & Dahleh, 1994). Reducing the dynamical uncertainty of the system would allow better prediction of the dynamical behavior of the system and therefore allow both faster and more accurate AFM imaging.

Acknowledgments

This work has been supported by the Netherlands Organization for Scientific Research (NWO) under the Innovational Research Incentives Scheme (VENI DOV.7835) and by the National Institutes of Health under Award NIH RO1 GM 065354. The authors would like to thank C.J. Slinkman, and A. Kunnappillil Madhusudhanan of the Delft University of Technology for their support on the development of the electronics used in this research.

References

Alexander, S., Hellemans, L., Marti, O., Schneir, J., Elings, V., Hansma, P., et al. (1989). An atomic-resolution atomic-force microscope implemented using an optical lever. *Journal of Applied Physics*, *65*, 164–167.

Ando, T., Kodera, N., Takai, E., Maruyama, D., Saito, K., & Toda, A. (2001). A high-speed atomic force microscope for studying biological macromolecules. *Proceedings of the National Academy of Sciences*, *98*, 12468–12472.

Binnig, G., Quate, C., & Gerber, C. (1986). Atomic force microscope. *Physical Review Letters*, *56*, 930–933.

Blom, R., & Van den Hof, P. (2010). Multivariable frequency domain identification using IV-based linear regression. In *49th IEEE conference on decision and control* (pp. 1148–1153), Atlanta, USA, IEEE.

de Callafon, R., Nagamune, R., & Horowitz, R. (2006). Robust dynamic modeling and control of dual-stage actuators. *IEEE Transactions on Magnetics*, *42*, 247–254.

Croft, D., Shed, G., & Devasia, S. (2001). Creep, hysteresis, and vibration compensation for piezoactuators: *Atomic force microscopy applications*. *AMSE Journal of Dynamic Systems, Measurement, and Control*, *123*, 35–43.

Easton, P., & West, P. (2010). *Atomic force microscopy*. Oxford University Press.

Fleming, A. (2010). Quantitative SPM topographies by charge linearization of the vertical actuator. *Review of Scientific Instruments*, *81*(1–5), 103701.

Fleming, A., Kenton, B., & Leang, K. (2010). Bridging the gap between conventional and video-speed scanning probe microscopes. *Ultramicroscopy*, *110*, 1205–1214.

Van Hulzen, J. R.., Schitter, G., Van den Hof, P. M. J., & Van Eijk, J. (2012). Dynamics, load balancing, and modal control of piezoelectric tube actuators. *Mechatronics*, *22*(3), 282–294.

Jeong, Y., Jayanth, G., Jhiang, S., & Menq, C. (2006). Direct tip–sample interaction force control for the dynamic mode atomic force microscopy. *Applied Physics Letters*, *88*, 204102.

Kinney, C., de Callafon, R., & de Oliveira, M. (2007). Spectral over-bounding of frequency data for modeling product variability in hard disk drive actuators. In *Proceedings of the European control conference 2007* (pp. 2902–2907), Kos, Greece.

Knebel, D., Amrein, M., Voigt, K., & Reichelt, R. (1997). A fast and versatile scan unit for scanning force microscopy. *Scanning*, *19*, 264–268.

Kuiper, S., Van den Hof, P., & Schitter, G. (2012). Trade-off between the control bandwidth and the measurement accuracy in atomic force microscopy. In *Proceedings of the 2012 IEEE international instrumentation and measurement technology conference*, 13–16 May 2012, Graz, Austria.

Kuiper, S., & Schitter, G. (2010). Active damping of a piezoelectric tube scanner using self-sensing piezo actuation. *Mechatronics*, *20*, 656–665.

Lee, C., & Salapaka, S. (2010). Fast imaging with alternative signal for dynamic atomic force microscopy. *Applied Physics Letters*, *97*, 133101.

Merry, R., Uyanik, M., van de Molengraft, R., Koops, R., van Veghel, M., & Steinbuch, M. (2009). Identification, control and hysteresis compensation of a 3 DOF metrological AFM. *Asian Journal of Control*, *11*, 130–143.

Pintelon, R., & Schoukens, J. (2001). *System identification: A frequency domain approach*. Wiley-IEEE Press.

Sahoo, D., Sebastian, A., & Salapaka, M. (2003). Transient-signal-based sample-detection in atomic force microscopy. *Applied Physics Letters*, *83*, 5521.

Salapaka, S., De, T., & Sebastian, A. (2005). A robust control based solution to the sample-profile estimation problem in fast atomic force microscopy. *International Journal of Robust and Nonlinear Control*, *15*, 821–838.

Sarid, D. (1994). *Scanning force microscopy*. New York: Oxford University Press.

Scheid, R., & Bayard, D. (1995). A globally optimal minimax solution for spectral overbounding and factorization. *IEEE Transactions on Automatic Control*, *40*, 712–716.

Schitter, G., Aström, K., DeMartini, B., Thurner, P., Turner, K., & Hansma, P. (2007). Design and modeling of a high-speed AFM-scanner. *IEEE Transactions on Control Systems Technology*, *15*, 906–915.

Schitter, G., Menold, P., Knapp, H., Allgöwer, F., & Stemmer, A. (2001). High performance feedback for fast scanning atomic force microscopes. *Review of Scientific Instruments*, *72*, 3320.

Schitter, G., Stemmer, A., & Allgöwer, F. (2004). Robust two-degree-of-freedom control of an atomic force microscope. *Asian Journal of Control*, *6*, 156–163.

Skogestad, S., & Postlethwaite, I. (2005). *Multivariable feedback control: Analysis and design*. John Wiley & Sons.

Tamer, N., & Dahleh, M. (1994). Feedback control of piezoelectric tube scanners. In *Proceedings of the 33th conference on decision and control*, Lake Buena Vista, FL, USA.

Trumper, D., Hocken, R., Amin-Shahidi, D., Ljubicic, D., & Overcash, J. (2011). High-accuracy atomic force microscope. In: E. Eleftheriou, & S. Moheimani (Eds.), *Control technologies for emerging micro and nanoscale systems. Lecture notes in control and information sciences*, Vol. 413 (pp. 17–46). Berlin/Heidelberg: Springer.

Vaseghi, S. (2009). *Advanced digital signal processing and noise reduction*. Wiley.